H.E.S.S. Collaboration, A. Abramowski... N. Maxted... B. Nicholas... G. Rowell... et al.

Identification of HESS J1303-631 as a pulsar wind nebula through γ-ray, X-ray, and radio observations

http://hdl.handle.net/2440/74976

Astronomy & Astrophysics

Identification of HESS J1303−631 as a pulsar wind nebula through γ-ray, X-ray, and radio observations

H.E.S.S. Collaboration, A. Abramowski[1], F. Acero[2], F. Aharonian[3,4,5], A. G. Akhperjanian[6,5], G. Anton[7], S. Balenderan[8], A. Balzer[7], A. Barnacka[9,10], Y. Becherini[11,12], J. Becker[13], K. Bernlöhr[3,14], E. Birsin[14], J. Biteau[12], A. Bochow[3], C. Boisson[15], J. Bolmont[16], P. Bordas[17], J. Brucker[7], F. Brun[12], P. Brun[10], T. Bulik[18], I. Büsching[19,13], S. Carrigan[3], S. Casanova[19,3], M. Cerruti[15], P. M. Chadwick[8], A. Charbonnier[16], R. C. G. Chaves[10,3], A. Cheesebrough[8], G. Cologna[20], J. Conrad[21], C. Couturier[16], M. Dalton[14,33], M. K. Daniel[8], I. D. Davids[22], B. Degrange[12], C. Deil[3], H. J. Dickinson[21], A. Djannati-Ataï[11], W. Domainko[3], L. O'C. Drury[4], G. Dubus[23], K. Dutson[24], J. Dyks[9], M. Dyrda[25], K. Egberts[26], P. Eger[7], P. Espigat[11], L. Fallon[4], C. Farnier[21], S. Fegan[12], F. Feinstein[2], M. V. Fernandes[1], A. Fiasson[27], G. Fontaine[12], A. Förster[3], M. Füßling[14], M. Gajdus[14], Y. A. Gallant[2], T. Garrigoux[16], H. Gast[3], L. Gérard[11], B. Giebels[12], J. F. Glicenstein[10], B. Glück[7], D. Göring[7], M.-H. Grondin[3,20], S. Häffner[7], J. D. Hague[3], J. Hahn[3], D. Hampf[1], J. Harris[8], M. Hauser[20], S. Heinz[7], G. Heinzelmann[1], G. Henri[23], G. Hermann[3], A. Hillert[3], J. A. Hinton[24], W. Hofmann[3], P. Hofverberg[3], M. Holler[7], D. Horns[1], A. Jacholkowska[16], C. Jahn[7], M. Jamrozy[28], I. Jung[7], M. A. Kastendieck[1], K. Katarzyński[29], U. Katz[7], S. Kaufmann[20], B. Khélifi[12], D. Klochkov[17], W. Kluźniak[9], T. Kneiske[1], Nu. Komin[27], K. Kosack[10], R. Kossakowski[27], F. Krayzel[27], H. Laffon[12], G. Lamanna[27], J.-P. Lenain[20], D. Lennarz[3], T. Lohse[14], A. Lopatin[7], C.-C. Lu[3], V. Marandon[3], A. Marcowith[2], J. Masbou[27], G. Maurin[27], N. Maxted[30], M. Mayer[7], T. J. L. McComb[8], M. C. Medina[10], J. Méhault[2], U. Menzler[13], R. Moderski[9], M. Mohamed[20], E. Moulin[10], C. L. Naumann[16], M. Naumann-Godo[10], M. de Naurois[12], D. Nedbal[31], D. Nekrassov[3], N. Nguyen[1], B. Nicholas[30], J. Niemiec[25], S. J. Nolan[8], S. Ohm[32,24,3], E. de Oña Wilhelmi[3], B. Opitz[1], M. Ostrowski[28], I. Oya[14], M. Panter[3], M. Paz Arribas[14], N. W. Pekeur[19], G. Pelletier[23], J. Perez[26], P.-O. Petrucci[23], B. Peyaud[10], S. Pita[11], G. Pühlhofer[17], M. Punch[11], A. Quirrenbach[20], M. Raue[1], A. Reimer[26], O. Reimer[26], M. Renaud[2], R. de los Reyes[3], F. Rieger[3,34], J. Ripken[21], L. Rob[31], S. Rosier-Lees[27], G. Rowell[30], B. Rudak[9], C. B. Rulten[8], V. Sahakian[6,5], D. A. Sanchez[3], A. Santangelo[17], R. Schlickeiser[13], A. Schulz[7], U. Schwanke[14], S. Schwarzburg[17], S. Schwemmer[20], F. Sheidaei[11,19], J. L. Skilton[3], H. Sol[15], G. Spengler[14], Ł. Stawarz[28], R. Steenkamp[22], C. Stegmann[7], F. Stinzing[7], K. Stycz[7], I. Sushch[14], A. Szostek[28], J.-P. Tavernet[16], R. Terrier[11], M. Tluczykont[1], K. Valerius[7], C. van Eldik[7,3], G. Vasileiadis[2], C. Venter[19], A. Viana[10], P. Vincent[16], H. J. Völk[3], F. Volpe[3], S. Vorobiov[2], M. Vorster[19], S. J. Wagner[20], M. Ward[8], R. White[24], A. Wierzcholska[28], M. Zacharias[13], A. Zajczyk[9,2], A. A. Zdziarski[9], A. Zech[15], and H.-S. Zechlin[1]

(Affiliations can be found after the references)

ABSTRACT

Aims. The previously unidentified very high-energy (VHE; $E > 100$ GeV) γ-ray source HESS J1303−631, discovered in 2004, is re-examined including new data from the H.E.S.S. Cherenkov telescope array in order to identify this object. Archival data from the *XMM-Newton* X-ray satellite and from the PMN radio survey are also examined.
Methods. Detailed morphological and spectral studies of VHE γ-ray emission as well as of the *XMM-Newton* X-ray data are performed. Radio data from the PMN survey are used as well to construct a leptonic model of the source. The γ-ray and X-ray spectra and radio upper limit are used to construct a one zone leptonic model of the spectral energy distribution (SED).
Results. Significant energy-dependent morphology of the γ-ray source is detected with high-energy emission ($E > 10$ TeV) positionally coincident with the pulsar PSR J1301−6305 and lower energy emission ($E < 2$ TeV) extending ∼0.4° to the southeast of the pulsar. The spectrum of the VHE source can be described with a power-law with an exponential cut-off $N_0 = (5.6 \pm 0.5) \times 10^{-12}$ TeV^{-1} cm^{-2} s^{-1}, $\Gamma = 1.5 \pm 0.2$) and $E_{\mathrm{cut}} = (7.7 \pm 2.2)$ TeV. The pulsar wind nebula (PWN) is also detected in X-rays, extending ∼2−3′ from the pulsar position towards the center of the γ-ray emission region. A potential radio counterpart from the PMN survey is also discussed, showing a hint for a counterpart at the edge of the X-ray PWN trail and is taken as an upper limit in the SED. The extended X-ray PWN has an unabsorbed flux of $F_{2-10\,\mathrm{keV}} \sim 1.6^{+0.2}_{-0.4} \times 10^{-13}$ erg cm^{-2} s^{-1} and is detected at a significance of 6.5σ. The SED is well described by a one zone leptonic scenario which, with its associated caveats, predicts a very low average magnetic field for this source.
Conclusions. Significant energy-dependent morphology of this source, as well as the identification of an associated X-ray PWN from *XMM-Newton* observations enable identification of the VHE source as an evolved PWN associated to the pulsar PSR J1301−6305. This identification is supported by the one zone leptonic model, which suggests that the energetics of the γ-ray and X-ray radiation are such that they may have a similar origin in the pulsar nebula. However, the large discrepancy in emission region sizes and the low level of synchrotron radiation suggest a multi-population leptonic nature. The low implied magnetic field suggests that the PWN has undergone significant expansion. This would explain the low level of synchrotron radiation and the difficulty in detecting counterparts at lower energies, the reason this source was originally classified as a "dark" VHE γ-ray source.

Key words. Gamma rays: general – pulsars: individual: PSR J1301-6305 – ISM: individual objects: HESS J1303-631

1. Introduction

In recent years, nearly a hundred VHE γ-ray sources have been discovered by various experiments, including many different types of sources. Generally, sources from these different classes also exhibit radio and X-ray radiation, however, the discovery of TeV J2032+4130 by the HEGRA collaboration in 2002 (Aharonian et al. 2002) lead to a new class of extended Galactic VHE γ-ray sources without obvious counterparts at other wavelengths. HESS J1303−631, serendipitously discovered by H.E.S.S. (High Energy Stereoscopic System) during an observation campaign of the pulsar PSR B1259−63 (Aharonian et al. 2005a), in observations taken between January and June of 2004 (Aharonian et al. 2005b). HESS J1303−631 was the first so-called "dark source" discovered by H.E.S.S. More of these sources were discovered by the H.E.S.S. Collaboration in the following years (Aharonian et al. 2008; Tibolla et al. 2009). Identifying and understanding this new class of sources has become an important task for modern γ-ray astronomy.

A growing number of extended VHE γ-ray sources, without (or with significantly fainter or less extended) X-ray/radio counterparts, appear to be associated with energetic pulsars in the Galactic plane. Some recent examples of this class of objects include HESS J1825−137 (Aharonian et al. 2006a) and HESS J1356−645 (Abramowski et al. 2011). These associations are believed to represent pulsar wind nebulae (PWNe), which are thought to be powered by a relativistic lepton-dominated particle outflow from a central pulsar. Many of these PWN associations form what are known as offset PWNe where the pulsar is located at or near the edge of the γ-ray and X-ray emission regions. These configurations may form in two ways. First, a high spatial velocity pulsar, possibly supersonic (in which case a bow shock nebula may form), leaves behind a "trail" of high-energy electrons in the ambient medium. Alternatively, an offset PWN may form if its expansion is blocked on one side by the reverse shock of the supernova remnant (SNR) in which the pulsar was born. Due to inhomogeneous densities in the ISM, the expansion of the supernova remnant may proceed asymmetrically, or the motion of the pulsar may place it near the edge of the SNR and the expanding PWN may then be disrupted asymmetrically by the reverse shock of the SNR, a scenario known as a crushed PWN (Blondin et al. 2001).

At the time of discovery, HESS J1303−631 was found to have a large intrinsic Gaussian extent of ∼0.16°, assuming a 2-dimensional symmetric Gaussian distribution, and a flux of ∼17% of the Crab flux above 380 GeV. Originally, the source had no known extended counterparts at other wavelengths and was, therefore, classified as a dark source. As is the case with many such dark sources, HESS J1303−631 is found to have a pulsar lying near the edge of the emission region with a high enough spin-down luminosity to account for the γ-ray emission. PSR J1301−6305 is located at the northwestern edge of the emission region of the H.E.S.S. source and, with a spin-down luminosity $\dot{E}$ = 1.7×10^{36} erg s^{-1}, is the most powerful pulsar within 6° of the H.E.S.S. source (Manchester et al. (2005), see Table 1 for a list of known pulsars within 0.5° of HESS J1303−631). This pulsar is young, with a characteristic age of τ_c = 11 kyr, and a rotation period of 184 ms.

Originally, the distance to PSR J1301−6305 was estimated to be 15.8 kpc, based on Taylor & Cordes (1993), which would have required a rather high γ-ray conversion efficiency of 37% in the 0.3 to 10 TeV range. Using a newer model of the Galactic electron distribution, NE2001 (Cordes & Lazio 2002), however, yields a much closer distance of 6.6 kpc. Using this updated

Table 1. All known pulsars within 0.5° of HESS J1303−631 (Manchester et al. 2005).

Pulsar	$\dot{E}/10^{30}$ erg/s	$\delta_{10\ \mathrm{TeV}}$ [arcmin]
PSR J1301−6305	1 700 000	3.1
PSR J1301−6310	6800	6.6
PSR J1305−6256	760	24.2
PSR J1302−6313	270	7.2
PSR J1303−6305	7	5.6

Notes. $\delta_{10\ \mathrm{TeV}}$ is the distance from the given pulsar to the $E > 10$ TeV peak position.

distance estimate, the reported VHE γ-ray spectrum at the time of discovery yields an integrated flux in the 1 to 30 TeV band of Φ = 1.2×10^{-11} erg cm^{-2} s^{-1} or 3.7% of the current spin-down luminosity of this pulsar, ($F_{6.6} = \dot{E}/4\pi(6.6 \text{ kpc})^2 = 3.26 \times 10^{-10}$ erg cm^{-2} s^{-1}), a γ-ray conversion efficiency which is comparable to other VHE PWNe (typically 0–7%, see e.g. Mattana et al. 2009).

A 5 ks *Chandra* X-ray observation, partially covering the VHE peak emission region (Mukherjee & Halpern 2005), revealed several point sources within the field of view, but no extended emission corresponding to the γ-ray emission region was found, and none of the radio pulsars in the field of view of the *Chandra* observation were detected. The possibility of an annihilating clump of dark matter as the origin of the γ-ray signal was explored by Ripken et al. (2008). Such a model could explain the lack of detection of lower energy counterparts. However, it was found that the spectrum obtained for this source would require an unreasonably high mass for the candidate dark matter particles (∼40 TeV). Also, as mentioned in that study, the inferred lateral density distribution does not support a dark matter scenario. Ripken et al. (2008), therefore, concluded this to be an unlikely candidate for the explanation of the VHE source.

To build a complete picture of the γ-ray emission process in this source, data from recent re-observations of HESS J1303−631 with the H.E.S.S. telescope array were analysed, enabling studies of energy-dependent morphology. Also, follow-up observations by the *XMM-Newton* X-ray satellite, performed in 2005, showing a detection of a compact source slightly offset from the pulsar position and a significantly extended PWN, are presented.

In Sect. 2, the H.E.S.S. instrument, data and analysis methods are discussed as well as the light curve. Section 3 describes the studies of energy-dependent morphology of the γ-ray source, followed by a discussion of the spectrum of the source in Sect. 4. Section 5 presents the results of the *XMM-Newton* X-ray follow-up observations, showing an X-ray PWN associated with the pulsar PSR J1301−6305. Finally, in Sect. 6, the implications of the analysis are discussed and the case is made for an association of HESS J1303−631 with the pulsar PSR J1301−6305.

2. H.E.S.S. observations and analysis

2.1. The H.E.S.S. instrument

H.E.S.S. is an array of four imaging atmospheric Cherenkov telescopes located in the Khomas Highland of Namibia (23°16′18″ S, 16°30′00″ E) at an altitude of 1800 m above sea-level. The telescopes image the Cherenkov light emitted by charged particles in the extensive air shower created when a γ-ray is absorbed in the atmosphere. They are optimized for detection of VHE γ-ray initiated showers in the energy range of

hundreds of GeV to tens of TeV by Each telescope has a 107 m² tessellated mirror surface and is equipped with a 960 photomultiplier tube camera with a field of view (FoV) diameter of ∼5° (Bernlöhr et al. 2003; Cornils et al. 2003). The telescopes are triggered in coincidence mode (Funk et al. 2004) assuring that an event is always recorded by at least two of the four telescopes allowing stereoscopic reconstruction of the showers. More information about H.E.S.S. can be found in Hinton (2004).

## 2.2. Data and analysis techniques

HESS J1303−631 was originally discovered during an observation campaign for PSR B1259−63. Follow-up observations of the two sources between 2004 and 2008 led to a total dataset of 108.3 h of live time, using only observations which passed standard H.E.S.S. data quality selection which rejects observations taken during periods of bad weather or with instrumental irregularities. The data were taken in wobble mode at an average zenith angle of 43.8°, with an average offset of 0.8° from the position reported in the discovery paper (Aharonian et al. 2005b).

The data were analyzed using H.E.S.S. standard Hillas reconstruction (Aharonian et al. 2006b). Cuts were applied to the shower image parameters to minimize background, primarily due to cosmic-ray protons. For spectrum extraction, standard cuts (also defined in Aharonian et al. 2006b), were used together with the Reflected-Region Background method (Berge et al. 2007) to subtract residual cosmic ray background, which resulted in an average energy threshold of ∼720 GeV. The resulting excess for this analysis was found to be 12085 photons for a detection significance of 33σ. Some of these early observations were made with telescope pointings coincident with the HESS J1303−631 emission region, rendering them unsuitable for spectral analysis since placement of reflected regions for background estimation is not possible. For the morphology studies, hard cuts were applied to further reduce background contamination and improve image reconstruction, and hence the point spread function (PSF) of the instrument, at the expense of a higher energy threshold, together with the Ring Background method, resulting in an average energy threshold of ∼840 GeV. Cross-checks were performed using a multi-variate analysis (Ohm et al. 2009), with background suppression based on boosted-decision trees, leading to compatible results.

2.3. VHE γ-ray map and light curve

The VHE γ-ray excess map (Fig. 1) of the HESS J1303−631 FoV shows extended emission to the southeast of PSR J1301−6305. A fit of a two-dimensional asymmetric Gaussian function to the excess resulted in a best-fit position of $\alpha = 13^{\rm h}02^{\rm m}48^{\rm s} \pm 3^{\rm s}_{\rm stat}$, $\delta = -63°10'39'' \pm 24''_{\rm stat}$ (J2000.0), with major/minor axis Gaussian widths of $\sigma_{\rm x} = 0.194° \pm 0.008°$ and $\sigma_{\rm y} = 0.145° \pm 0.006°$, with a position angle (counter clockwise from north) of $\phi = 147° \pm 6°$. The $\chi^2/N.D.F.$ of the fit was 390/391. The exposure gradient over the source extension was found to be small and have a negligible affect on the resulting source position. The fitted position is consistent with the one quoted in the original discovery paper (Aharonian et al. 2005b), but slightly shifted towards the pulsar position due to the (compared to the discovery paper) higher energy threshold of the hard cuts used and the presence of energy-dependent morphology (see Sect. 3).

The nightly flux was determined using a flux extraction region of radius 0.6° to ensure full enclosure of the source, around
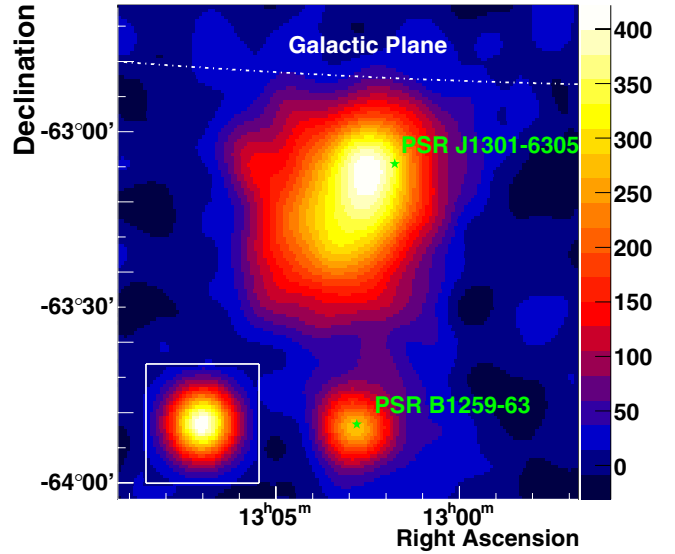

Fig. 1. The HESS J1303−631 VHE γ-ray excess map, produced using hard cuts and the ring background method, was smoothed with a Gaussian kernel with $\sigma = 0.05°$. Coordinates are J2000.0. The high spin-down power pulsar, PSR J1301−6305, is indicated with a green star to the northwest of HESS J1303−631. The point source, associated to the pulsar PSR B1259−63, is seen in the bottom of the FoV. The size of the H.E.S.S. PSF, also smoothed with a Gaussian kernel with $\sigma = 0.05°$, is shown in the white box to the lower left. The blue/red transition occurs at a detection significance of ∼5σ.

the best fit position given above assuming a power-law spectrum with an index of 1.5. Studies were performed to account for influences from the nearby VHE source PSR B1259−63. As expected for an extended source, with an estimated diameter of 40 pc at a distance of 6.6 kpc, the nightly flux is consistent with constant emission, with $\chi^2/N.D.F. = 77/69$, verifying the stability of the H.E.S.S. instrument over the period of data taking.

3. Energy-dependent morphology

To test for the presence of energy-dependent morphology in the VHE source, excess images were generated in the following energy bands: $E_1 = (0.84-2)$ TeV, $E_2 = (2-10)$ TeV and $E_3 > 10$ TeV (Fig. 2, left, top to bottom). The radial acceptance of the FoV was determined from the data, thus naturally accounting for the energy dependence. Slices were made on the uncorrelated excess images having dimensions of $1.0° \times 0.1°$ and centered at the best fit position of the VHE excess. The orientation is chosen along the fitted position angle (see Sect. 2.2). A Gaussian function was then fit to each slice as shown in Fig. 2 (right). The intrinsic source width was obtained by fitting the convolution of a Gaussian with the energy dependent H.E.S.S. PSF.

The resulting parameters of the PSF convolved Gaussian fits, mean c and intrinsic Gaussian width $w_{\rm int}$, for each energy band (Table 2) were then plotted as a function of energy (Fig. 3). A fit of a constant to these parameters yielded very bad quality fits, which establishes the existence of strong energy-dependent morphology. This morphology implies a spectral steepening in γ-rays away from the pulsar, a physical property predicted to be present in evolved PWNe. Fitting a linear function yielded much better quality fits (Table 3) and a model of the morphology parameterized by a projected center of emission, $c(E)$, calculated with respect to the pulsar position, and an intrinsic source Gaussian width, $w_{\rm int}(E)$, which is calculated by taking
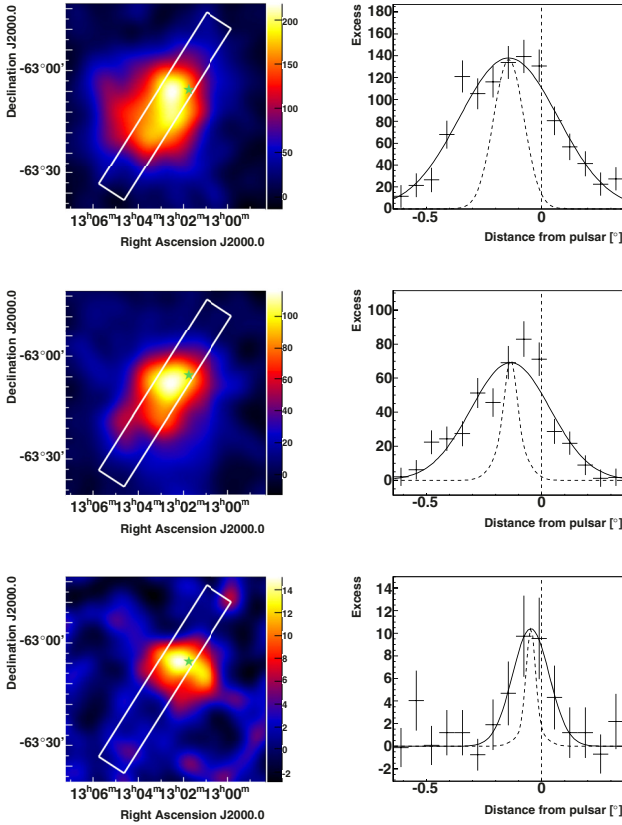
Fig. 2. *Left*: uncorrolated excess images of the HESS J1303−631 region in the energy bands $E_1 = (0.84−2)$ TeV, $E_2 = (2−10)$ TeV and $E_3 > 10$ TeV (from *top to bottom*). Coordinates are J2000.0. All images were smoothed with a Gaussian kernel of width 0.05°. Slices are indicated by the rectangles, taken in the direction of the semi-major axis of the fitted asymmetric Gaussian function. *Right*: the slices on the uncorrelated excess images are then fitted with a Gaussian function. The pulsar position is marked by a green star in the sky maps and a dashed line in the profiles. The dashed curves show the energy-dependent PSF of the H.E.S.S. instrument.

into account the (energy-dependent) finite angular resolution of the instrument:

$$c = (0.157 \pm 0.012)° − (0.006 \pm 0.002)° \times E_{\text{TeV}}$$
$$w_{\text{int}} = (0.215 \pm 0.012)° − (0.009 \pm 0.002)° \times E_{\text{TeV}}.$$

4. Energy spectrum

The spectrum was derived using the Reflected-Region background method with an integration region of radius 0.6°, roughly three times the intrinsic Gaussian extent at low energies to avoid effects of energy-dependent morphology, centered at the fitted source position. The derived spectrum for the entire dataset, excluding observations where the offset of the pointing position to the center of the source is less than 0.6° (reducing the total live time to 70.3 h), is shown in Fig. 4. The spectrum was fit with a power-law function, $dN/dE = N_0(E/1\,\text{TeV})^{-\Gamma}$, with a resulting photon index of $\Gamma = 2.44 \pm 0.03_{\text{stat}}$ and a normalization constant $N_0 = (5.9 \pm 0.3_{\text{stat}}) \times 10^{-12}$ TeV^{-1} cm^{-2} s^{-1}. This normalization is larger than that found in the original discovery paper due to a larger integration region. However, with the inclusion of the additional data taken since the source discovery, the p-value of a chi-squared minimization is rather poor (7×10^{-8}). A chi-square

Table 2. Results of the Gaussian fit to the slices on the excess images in the energy bands $E_1 = (0.84–2)$ TeV, $E_2 = (2–10)$ TeV and $E_3 > 10$ TeV.

Band	c	w_{img}	w_{int}	P
E_1	$−0.14° \pm 0.01°$	$0.21° \pm 0.01°$	$0.20° \pm 0.01°$	0.42
E_2	$−0.13° \pm 0.01°$	$0.17° \pm 0.01°$	$0.16° \pm 0.01°$	0.14
E_3	$−0.05° \pm 0.02°$	$0.08° \pm 0.02°$	$0.07° \pm 0.02°$	0.97

Notes. c is the mean of the Gaussian, w_{img} is the Gaussian width and w_{int} is the intrinsic Gaussian width of the source after correcting for the PSF, P is the p-value of the χ^2 fit.
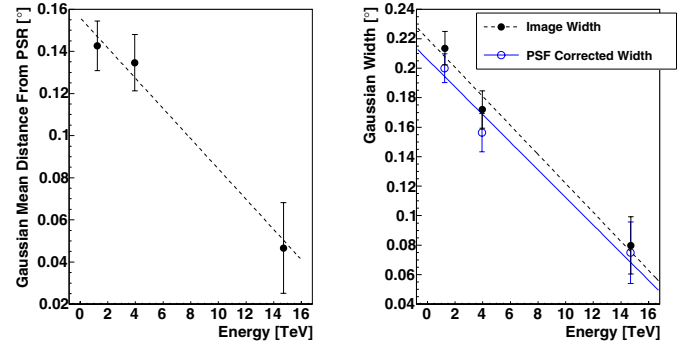
Fig. 3. *Left*: HESS J1303−631 fitted Gaussian mean, $c(E)$, measured from the pulsar position, as a function of energy. *Right*: the PSF corrected intrinsic Gaussian extension ($w_{\text{int}}(E)$, blue) is overlaid with the fitted uncorrected excess Gaussian extension ($w_{\text{img}}(E)$, black dashed) as a function of energy. The points are placed at the average energy of the photons falling in the corresponding energy bin (indicated by the horizontal error bars, not used in fit).

Table 3. Quality of fit of a constant vs. a line to the source intrinsic Gaussian extension and mean, measured from the pulsar position, as a function of energy.

Constant fit	$\chi^2/N.D.F.$	p-value
w_{int}	44.9/2	1.8×10^{-10}
c	18.3/2	1.1×10^{-4}
Linear fit		
w_{int}	0.4/1	0.55
c	2.4/1	0.12

Notes. The much improved p-values of the linear fits as compared to the constant fits indicate the presence of significant energy-dependent morphology.

fit to a power-law spectrum with a cut-off at the energy E_{cut},

$$\frac{dN}{dE} = N_0 E^{-\Gamma} e^{-E/E_{\text{cut}}},$$

yielded a better p-value of 1%, with fitted parameters $N_0 = (5.6 \pm 0.5_{\text{stat}}) \times 10^{-12}$ TeV^{-1} cm^{-2} s^{-1}, $\Gamma = 1.5 \pm 0.2_{\text{stat}}$ and $E_{\text{cut}} = (7.7 \pm 2.2_{\text{stat}})$ TeV. This spectrum yields an integrated flux in the 1–30 TeV band of $(2.5 \pm 0.1) \times 10^{-11}$ erg cm^{-2} s^{-1} or 7.7% of $F_{6.6}$. Monte-Carlo studies were preformed to test for a possible contribution from the source PSR B1259−63 (spill over events), due to the position and size of the integration region and the exclusion region for PSR B1259−63. Effects from this source are estimated to be about 2% on the integrated flux, smaller than statistical and systematic errors.
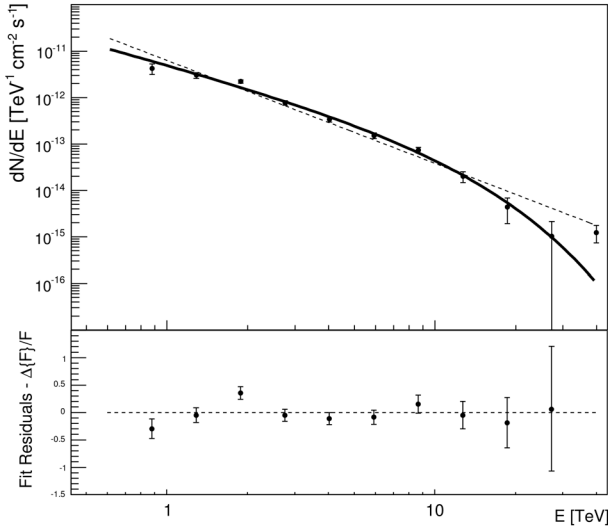
Fig. 4. HESS J1303−631 spectrum derived using an integration region of radius 0.6°. The spectrum is well fit with a power-law function with spectral index $\Gamma = 1.5 \pm 0.2$ with a fitted cutoff energy of $E_{\text{cut}} = (7.7 \pm 2.2)$ TeV. The fit resulted in a $\chi^2/N.D.F.$ of (20/8) corresponding to 1% p-value. A fit of a power-law spectrum with no cutoff, shown by the dashed line, resulted in a p-value of 7×10^{-8}. The last spectrum point deviates $\sim 2\sigma$ from the fitted curve. It was removed from the residuals plot for better visibility.

5. *XMM-Newton* X-ray observations

In a search for counterparts of the VHE γ-ray source in the keV energy band, two *XMM-Newton* observations, each about 30 ks, were carried out on July 12th and 14th, 2005, in satellite revolution number 1024 (ObsID 0303440101, "Observation 1") and revolution 1025 (ObsID 0302340101, "Observation 2") respectively. All three X-ray imaging CCD cameras (EPIC MOS1, MOS2, and pn) were operated in full-frame mode, with a medium filter to screen out optical and UV light, with the exception of the pn camera during the first observation, where the large window mode with the Thin1 filter was used.

5.1. Data analysis

For the data analysis of these observations, the *XMM-Newton* Science Analysis Software (SAS), version 9.0, was used (http://xmm.esac.esa.int/sas/). Cleaning the data and removing periods of high background due to soft proton flares resulted in a combined data set of about 52 ks exposure. For this analysis, the energy band 2–8 keV was used to optimize the signal-to-noise ratio, since few events are expected at lower energies due to high absorption. The SAS task emosaicproc was used to combine the observations and perform source detection, resulting in the detection of 73 point sources within the combined field of view above the maximum likelihood threshold of 10. The X-ray PWN associated to PSR J1301−6305 was also detected in this way, corresponding to the 2XMMi catalog source 2XMM J130145.7−630536 (Watson et al. 2009), with a flux of $F_{2-12\,\text{keV}} = (7.7 \pm 1.0) \times 10^{-14}$ erg cm^{-2} s^{-1} but peaked 15″±1.6″ to the east of the pulsar with an extension of 6″ at a maximum likelihood of 7.7 (sources with likelihood <8 may be spurious). No emission corresponding to the full extension of the H.E.S.S. source was found. However, a small apparently extended asymmetric X-ray source, directly adjacent to PSR J1301−6305, is seen extending roughly 2′ from the pulsar position towards the
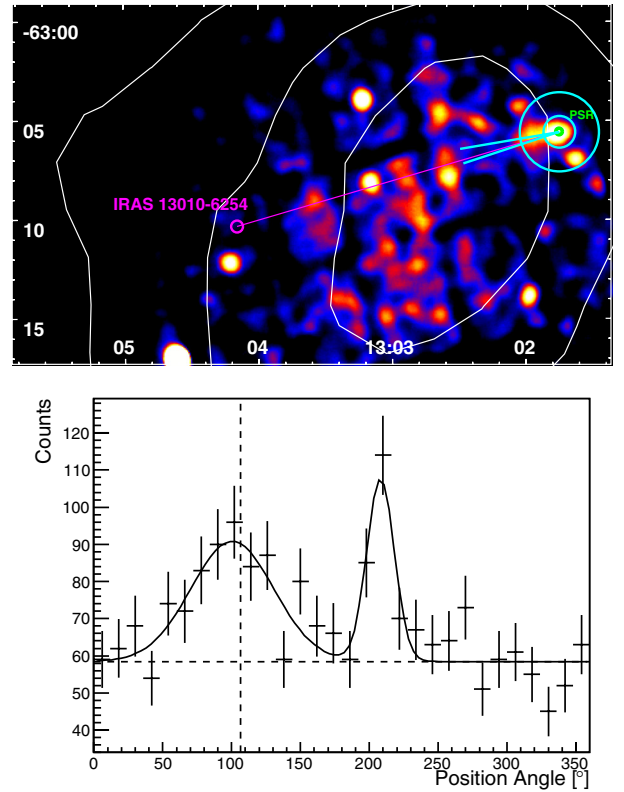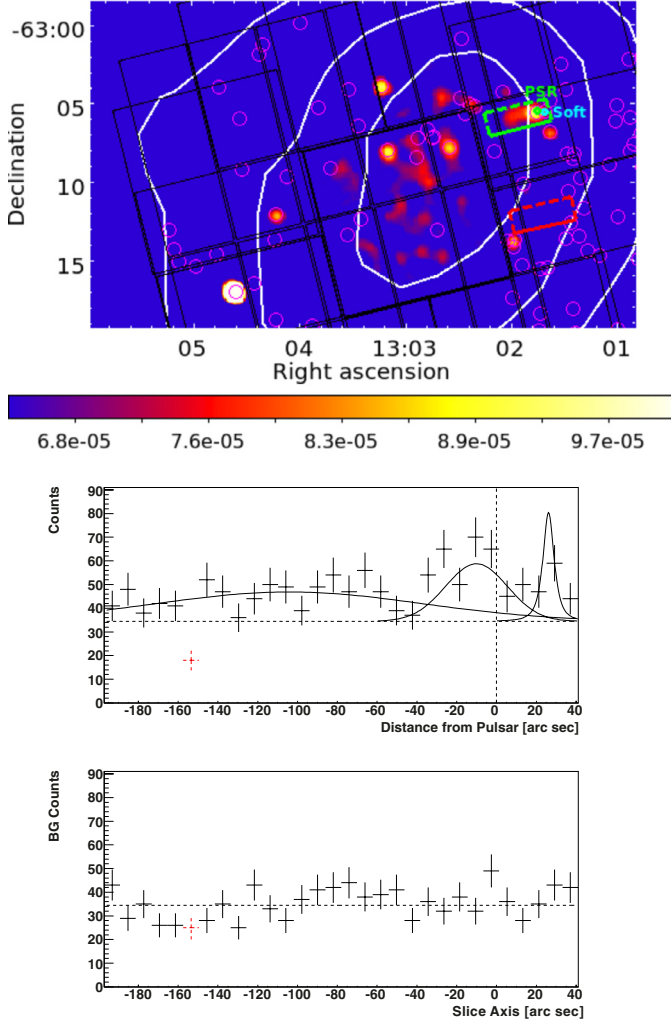

Fig. 5. *Top*: the 2–8 keV *XMM-Newton* X-ray count map in the region of the pulsar smoothed by a Gaussian kernel of width $\sigma = 40''$. The horizontal axis is Right Ascension and vertical axis is Declination in J2000.0 coordinates. The count map is not exposure corrected, thus the apparent enhanced emission near the center is only an artifact. Overlaid is the projection annulus, shown in cyan, used to determine the direction of the X-ray extension, with inner radius of 48″ and outer radius of 120″, centered on the pulsar position. The 8, 14 and 20σ TeV significance contours are shown in white. The direction of the extension is found to be within 1σ from the direction of the star formation region, IRAS 13010−6254, located at a position angle of 106.3°, indicated by a magenta line in the sky map and a dashed line in the projection. The cyan lines in the sky map show the 1σ errors in the fitted direction of the extension. *Bottom*: the X-ray azimuthal projection in position angle from the pulsar location. The projected on-counts were fitted with the sum of a Gaussian and a flat background giving a position angle of $101.5° \pm 5.3°$ and a Gaussian width of $30° \pm 7°$. The point source located at $\sim 210°$ is an unidentified X-ray source.

center of the VHE γ-ray emission region (Fig. 5). A detailed analysis of this feature is presented in the following section.

While Observation 1 has the pulsar position closer to on-axis than Observation 2, it is unfortunately not suited for studying the extended X-ray source since the extended region found in Observation 2 lies directly on/between the edges of the CCD chips in all three detectors in Observation 1, thereby obscuring the view of this feature. Therefore, only Observation 2 was used for further analysis.

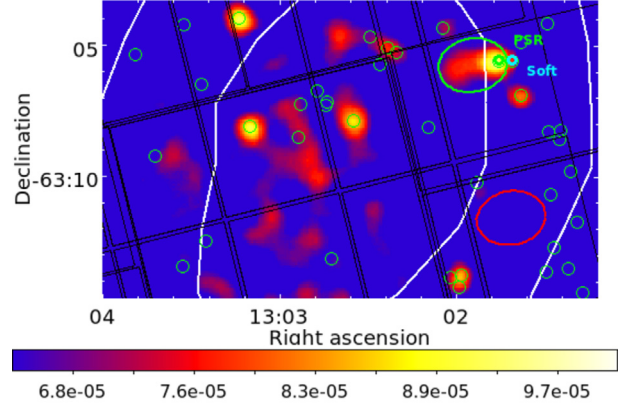### 5.2. Extended X-ray PWN

To determine the direction of the X-ray feature, possibly associated to PSR J1301−6305, an annular projection was taken around the pulsar position with an inner radius of 48″ and an outer radius of 120″ (Fig. 5 top). The projected counts were fitted with the sum of a Gaussian and a flat background giving a position angle of $101.5° \pm 5.3°$ and a Gaussian width of $30° \pm 7°$

top. This potential birthplace for the pulsar is considered in more detail in Sect. 7.

In order to determine the extension of the extended X-ray feature, a slice on the count map containing the pulsar was taken (Fig. 6, top) in the direction determined by the azimuthal projection, with a slice width of 88″ and a length of 238″ (on slice). A background slice of the same size and orientation was chosen in a source free region at roughly equal offset to the center of the FOV as the on slice to ensure equal exposure. The slices are completely contained within single chips in the MOS1 and MOS2 cameras and extend ∼40″ over the edges of neighboring chips in the pn camera. Profiles of the on slice and background slice are shown in Fig. 6 (middle and bottom).

A point source located just west of the pulsar, 2XMM J130141.3−630535, is presumably unrelated to the pulsar due to its soft nature (the hardness ratio R2, comparing the 1–2 keV to 0.5–1 keV bands, is 0.12 ± 0.08 compared to 0.76 ± 0.12 for the source associated to the pulsar).
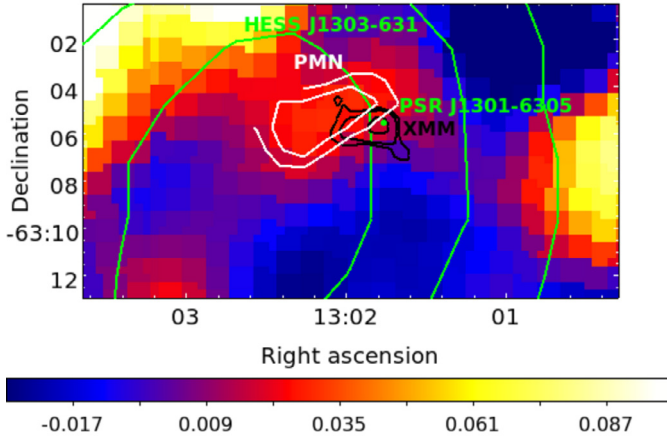
The slice (Fig. 6, middle) does not exhibit enough statistics to precisely determine the morphology of the X-ray extension, but the extension appears to consist of a more compact region near the pulsar position, referred to in this section as the "compact region", and extending ∼40″ to the left, corresponding to the 2XMMi catalog source 2XMM J130145.7−630536 as well as a feature extending from ∼−40″ to ∼−150″, referred to here as the "diffuse" emission region.

A simultaneous fit of the slices was performed, consisting of a fit to the unrelated soft point source to the west of the pulsar, a Gaussian to the "compact" region near the pulsar position, a larger Gaussian to the "diffuse" region extending to the east and a constant to the counts in the background slice. The fit resulted in a diffuse emission centered at −104″ ± 18″ with a Gaussian width of σ = 66″ ± 19″ while the compact region was found to be centered at −10″ ± 4″ with a width of 16″ ± 4″. The unrelated point source was fitted with a King profile

$$f(x) = \frac{C}{\left(1 + (\frac{x-x_0}{R_0})^2\right)^\alpha}, \tag{1}$$

with $R_0 = 4.3''$ and $\alpha = 1.5$, corresponding to the PSF of the *XMM-Newton* pn camera at 1.5 keV and at ∼10′ offset from the center of the field of view. For the other cameras, the PSF is slightly narrower than this.

The total X-ray extension is found to extend roughly 170″ (diffuse center +1σ width) beyond the pulsar position, however,

Fig. 6. Smoothed, exposure corrected *XMM-Newton* X-ray flux map (cm^{-2} s^{-1}) in the 2–8 keV energy band (*top*) The horizontal axis is Right Ascension and the vertical axis is Declination in J2000.0 coordinates. An extended X-ray source appears from the position of the pulsar, PSR J1301−6305 (green dot), and extends roughly in the direction of the center of the H.E.S.S. source (white contours show 8, 14 and 20σ γ-ray significance). Chip edges are shown in black for all three detectors and XMM catalog sources are shown in magenta. The green box shows the slice used to create the profile (*middle*) and the red box shows the slice used for background estimation (*bottom*). Both slices were taken from the un-exposure corrected count map. A presumably unrelated soft point source, 2XMM J130141.3−630535, is shown in the map as a cyan dot. The excess was simultaneously fit with two Gaussians (the "compact region" near the pulsar position plus the "diffuse region" left of the pulsar) a King profile for the unrelated soft source to the right of the pulsar position and a constant background from the bottom slice. The red dotted bins in the projections lie directly on a chip edge in the pn camera in both slices and are excluded from the analysis. The dashed horizontal line indicates the fitted background level.

(Fig. 5 bottom). The statistics were too low to warrant individual examination of the three cameras. The direction of the extension as determined here was used for the orientation of the slice on the count map, as presented below.

The direction of the X-ray extension is consistent to within 1σ with the direction of the star formation region IRAS 13010−6254, on the opposite side but within the 8σ significance contour of the VHE source, as indicated in Fig. 5

Fig. 8. 4.85 GHz radio image from the PMN Survey (beam size FWHM 7′) in the HESS J1303−631 region. The horizontal axis is Right Ascension and the vertical axis is Declination in J2000.0 coordinates and scale is Jy/beam. H.E.S.S. contours are shown in green, *XMM-Newton* X-ray contours are shown in black and the radio contours are shown in white. A radio feature peaks about 3′ east of the pulsar position, just beyond the extended *XMM-Newton* X-ray source and near the center of the H.E.S.S. γ-ray source at a peak value of 0.03 Jy/beam. The apparent position of the radio feature may be slightly shifted to the northeast due to a strong gradient in background from neighbouring sources.

the tail of the extension may be cut short by the edge of the pn chip. However, taking an integration region from the edge of the pn chip, to avoid effects of changing sensitivity across chips, to the pulsar position (avoiding the soft point source to the west), for a total integration length of 145″ gives total on-counts of 950, and total background counts 689 with the on/off area ratio $\alpha = 1$ for an excess of 261 corresponding to a detection significance of 6.5σ.

5.3. X-ray spectrum

For the spectral extraction, placement of a ring for background determination was not possible due to multiple nearby sources. A small elliptical region covering the extension region was taken and an identical ellipse was used for background extraction (Fig. 7). The extraction regions are well contained within single chips for the MOS and pn cameras. The spectra were obtained for the three cameras indepedently and then fit simultaneously.

The obtained spectrum was fit using the spectral fitting software XSPEC with an absorbed power-law model which yielded a column density $N_{\rm H} = 2.7^{+1.3}_{-1.1} \times 10^{22}$ cm^{-2}, a photon index $\Gamma = 2.0^{+0.6}_{-0.7}$, and a flux normalization at 1 keV of $6.2^{+10}_{-3.8} \times 10^{-5}$ keV^{-1} cm^{-2} s^{-1}. The integrated unabsorbed flux in the 2–10 keV energy band was found to be

$$F_{\rm 2-10\ keV} = 1.6^{+0.2}_{-0.4} \times 10^{-13}\ {\rm erg\ cm^{-2}\ s^{-1}}.$$

6. Radio observations

The region of HESS J1303−631 was covered by a survey of the southern sky by the Parkes, MIT and NRAO (PMN) radio telescopes at 4.85 GHz (Condon et al. 1993). Calibrated maps were obtained from the NASA SkyView online tool, shown in Fig. 8. There is a radio feature just east of the X-ray nebula and near the peak of the VHE source, the apparent position of which may be shifted slightly to the northeast due to a strong gradient in the

FOV from the strong unidentified radio sources to the northeast. The feature is found to have a peak flux of 0.03 Jy/beam. The flux resolution (rms) of the PMN survey is 0.01 Jy/beam so that the significance of this feature is only 3σ and is at the detection limit of the survey (and thus not reported in the catalog). Therefore, the flux is taken as an upper limit. The feature is consistent with the size of the PSF of the survey (7′ FWHM) in the northeast to southwest direction, but may be slightly elongated in the northwest to southeast direction, roughly parallel to the X-ray extension. Since the feature is not significant, no definitive conclusions about its morphology can be made.

Although it is unclear whether this radio feature does indeed represent a counterpart of the γ-ray and X-ray sources, since this lies in a rather complicated region of the radio sky, the location is promising due to its similarities with other known PWNe having a radio peak just beyond the X-ray nebula, as in, for example, PSR B1929+10 (Becker et al. 2006) and the much smaller scale example of the "Mouse" PWN (Gaensler et al. 2004). Further observations in radio may be able to determine more precisely the morphology and polarization of the feature in order to establish an association.

7. Discussion

7.1. Multi-wavelength situation

Having analysed the morphology and spectra in VHE γ-rays, X-rays and radio data available for the region, it is now possible to consider HESS J1303−631 in a full multi-wavelength scenario. First, an energy mosaic of the VHE emission was created using the three smoothed excess images from Fig. 2. These images were overlaid, as shown in Fig. 9, along with the contours of the extended X-ray PWN. This energy mosaic is rather reminiscent of the known *off-set PWN* association HESS J1825−137 (Aharonian et al. 2006a) where the low-energy VHE γ-ray emission region is quite extended with the pulsar laying towards the edge of emission and with the higher energy emission more compact and found centered closer to the pulsar.

Taking the spectra and fluxes obtained in previous sections, it is now possible to consider the SED of the source in a PWN scenario. Although a time-dependent model, including the evolution of the lepton populations over time, would be required to accurately describe the emission observed in the various wave bands, for simplicity, and due to the limited number of multi-wavelength data available, a simple stationary "one zone" leptonic model (Aharonian & Atoyan 1999) was used to fit the VHE γ-ray and X-ray spectra as well as the single PMN upper limit in radio (Fig. 10). The leptonic model assumes that the same electron population, with an energy distribution in the form of a single power-law with an exponential cut-off, creates radio and X-ray emission via synchrotron emission as well as VHE γ-rays via inverse Compton (IC) scattering on cosmic microwave background photons. Inclusion of IC scattering on infrared and optical target photons (as obtained from GALPROP (Moskalenko et al. 2002), assuming a pulsar distance of 6.6 kpc) had a negligible effect on the model parameters.

The fit of the radio upper limit, and the X-ray and γ-ray fluxes with this model yielded an electron spectral index of $\alpha = 1.8^{+0.1}_{-0.1}$, a cut-off energy of $E_{\rm cut} = 31^{+5}_{-4}$ TeV, a normalization of $K_{\rm e} = 3.7^{+8.1}_{-2.9} \times 10^6$ cm^{-2} and an average magnetic field of $1.4^{+0.2}_{-0.2}$ μG, which is similar to the inferred mean line-of-sight magnetic field strength of ∼2 μG, as determined from the pulsar's rotation measure (Crawford & Tiffany 2007), but larger than the magnetic field of ∼0.17 μG predicted by the γ-ray
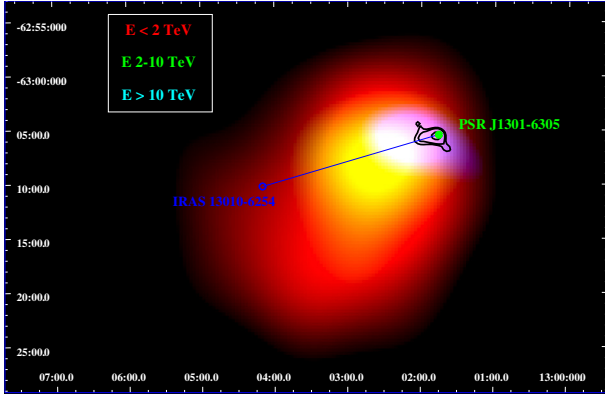
Fig. 9. Energy mosaic of HESS J1303-631. The horizontal axis is Right Ascension and the vertical axis is Declination in J2000.0 coordinates. Red: $E_1 = (0.84–2)$ TeV, green: $E_2 = (2–10)$ TeV and blue: $E_3 > 10$ TeV. The highest energy photons originate nearest the pulsar, PSR J1301−6305 (marked by the green dot). The visible red corresponds roughly to the 10-σ significance contour of the entire source. *XMM-Newton* X-ray contours are shown in black. A potential birthplace for the pulsar, IRAS 13010−6254, as indicated by the X-ray extension, is shown by a blue circle.

Fig. 10. Spectral Energy Distribution of HESS J1303−631 fitted with a simple stationary leptonic model. The required magnetic field is ~1.4 μG.

to X-ray luminosity scaling law given in Aharonian & Atoyan (1999). The p-value of the fit was 0.02 and the model predicts a total energy in electrons of $\sim 2.3 \times 10^{48}$ erg. It is worth noting that the resulting model spectrum in the radio band is steeper than typically observed in PWNe since the X-ray spectral index is not constrained and the fit of the single electron population is dominated by the narrow peak in TeV energies. Since the fluxes at the various energies described by this model are extracted from regions of differing size, the fitted magnetic field represents only an average and should be interpreted with caution.

The differing sizes of the γ-ray and X-ray emission regions imply the existence of differing electron populations so that the entire PWN cannot be accurately modeled by a single population. The simple approach presented here, therefore, suffers from the caveat that a model with two electron populations could reproduce the observed spectra with a significantly different magnetic field than obtained with a one zone model. Incorporating a strong cutoff in an older electron population at high energies would suppress the X-ray synchrotron emission, even in the face of a much higher magnetic field, and still reproduce the VHE peak. Indeed, the higher energy synchrotron emitting electrons may have been effectively extinguished precisely because of the high magnetic field. The morphology in VHE γ-rays shows no evidence of a distinct break in the populations of electrons caused by passage of an SNR shock, but rather appears to show a more continuous transition from lower to higher energies in VHE γ-rays and on up to the highest energy synchrotron X-ray emitting electrons closer to the pulsar. This would imply a continuous transition from older to younger electrons which may require not a two zone electron model, but a continuously changing population making modeling quite difficult. Due to scant spectra available at lower energies, the precise details of the electron populations cannot be distinguished, and this first order approximation model serves as a starting point for future studies and searches.

The VHE γ-ray morphology presented here favors the association of HESS J1303−631 with the high spin-down power pulsar PSR J1301−6305, which, on energetic grounds, is the only known association which can explain the TeV emission. Additionally, the detection of an extended asymmetric X-ray nebula in combination with a hint of a radio counterpart of the
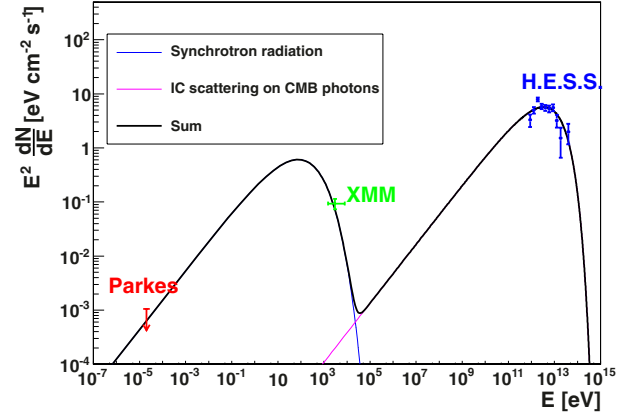
PWN seen in PMN observations, strengthens this association further.

7.2. Distance to the source

As stated before, the distance of 6.6 kpc to PSR J1301−6305 is based on the dispersion measure using the model of electron distribution in the Galaxy, a method which is often considered unreliable. For example, the "Mouse" pulsar has been argued to be at a distance roughly twice that determined by its dispersion measure based on the ratio of neutral hydrogen atoms to free electrons along the line of sight of $N_H/DM = 85$ which is much higher than the values seen for all other X-ray detected pulsars, for which typically we observe $N_H/DM \approx 5–10$ (Gaensler et al. 2004). For PSR J1301−6305, using the column density obtained here, we have $N_H/DM \sim 23$, one of the highest known N_H/DM ratios among PWNe, which could imply that the distance obtained from DM is an underestimate for this source as well.

On the other hand, the star formation region IRAS 13010−6254, if considered as a potential birthplace of the pulsar, provides an alternative estimation of the distance. The direction of the X-ray extension is found to be within 1σ from the direction of the star formation region, IRAS 13010−6254, located at a position angle of 106.3°, the only other identified object within the VHE emission region besides lower energy pulsars and stars. IRAS 13010−6254 has been identified as a point source in GeV γ-rays in Fermi observations by Wu et al. (2011) which could indicate the presence of evolved massive stars, which are the progenitors to pulsars, with colliding winds, or the presence of an SNR within the star forming region, or potentially a counterpart to a part of the VHE source given the bulge in the VHE significance contours at the position of the star forming region (see Fig. 5, top). As the only star formation region within more than a degree of the pulsar, and in the absence of another plausible SNR association, this provides a plausible candidate for the birthplace of the pulsar. This could be similar to the case of the X-ray feature G359.95−0.04 which was identified by Wang et al. (2006) as a PWN and found extending in the direction of the young stellar complex IRS 13, which was suggested as a possible birthplace for the yet undetected pulsar.

IRAS 13010−6254 has a kinematic velocity of $V_{SLR} = (33.4 \pm 3.2)$ km s^{-1} (Bronfman et al. 1996), which corresponds to a distance of ~12.4−12.9 kpc using the circular Galactic rotation

model of Brand & Blitz (1993) updated with the Galactic structure parameters of Reid et al. (2009). This is nearly double the distance of 6.6 kpc based on DM, placing the source close to the edge of the Galaxy. This kinematic distance is corroborated by the measure of the column density from X-rays, which is larger than the total integrated Galactic HI column density in that direction of 1.9×10^{22} cm^{-2} (Dickey & Lockman 1990).

If the pulsar was born in IRAS 13010−6254 then it would have traveled 0.28° or ∼62 pc, implying a very high transverse velocity of ∼5000 km s^{-1} if the characteristic age of 11 kyr is taken as the true age. This age estimate is, however, often considered to be unreliable and the true ages may differ by a factor of 2–3. The true age of the pulsar, assuming constant braking index, is given as (Manchester & Taylor 1977)

$$\tau = \frac{P}{(n-1)\dot{P}}\left[1 - \left(\frac{P_0}{P}\right)^{n-1}\right]. \qquad (2)$$

The characteristic age τ_c is calculated assuming a braking index of $n = 3$ (i.e. pure electro-magnetic braking) and that the birth period, P_0 is much less than the current period, P. The braking index has only been reliably measured for a handful of young pulsars (Alpar & Baykal 2006) and was found to be less than 3 in every case, with the extreme case of with $n = 1.4 \pm 0.2$ (Lyne et al. 1996) implying an age 5 times greater than predicted by τ_c if the assumption of $P_0 \ll P$ still holds, or PSR J1734−3333 with an index of $n = 0.9 \pm 0.2$ (Espinoza et al. 2011) implying an age which cannot be calculated with the above formula. Dupays et al. (2010) calculated the effects of quantum vacuum friction on the spindown of pulsars and found a braking index decreasing as $1 - (1 - n_0)e^{-At}$ with $A = \ddot{P}/\dot{P} + \dot{P}/P$ for period P and predict the braking index of the Crab pulsar at birth of just below 3 and that it will fall to ∼2 in the next 2 kyr from its current value of 2.5. Gaensler & Frail (2000) proposed that "characteristic ages greatly underestimate the true ages of pulsars" based on proper motion measurements of PSR B1757-24. On the other hand, Migliazzo et al. (2002) used proper motion measurements to show that the pulsar PSR B1951+32 is likely ∼40% younger than its characteristic age, implying a non-negligible birth period.

The very large "darkness ratio" of γ-ray to X-ray luminosity (in the 1–30 TeV and 2–10 keV bands respectively) for this source of 156, makes this the darkest identified PWN to date (the darker HESS J1702-420, darkness ratio 1500, is now believed to be an SNR, Giacani et al. 2011). This could imply a relatively old age for PSR J1301−6305. Mattana et al. (2009) considered the darkness ratios of PWNe and PWNe candidates detected by H.E.S.S., and found a logarithmic scaling with the characteristic age of the assumed associated pulsar. This scaling law predicts a darkness ratio of 6 for a pulsar with characteristic age 11 kyr, whereas the darkness ratio measured here would predict a characteristic age of 48 kyr, more than 4 times older.

A factor of 3 to 5 in the age of PSR J1301−6305 would bring the pulsar velocity down to ∼1600 to 1000 km s^{-1}. This high velocity is not unreasonable given the two component pulsar velocity model by Arzoumanian et al. (2002) which predicts ∼15% of all pulsars to have a space velocity greater than 1000 km s^{-1}, but would place PSR J1301−6305 among the fastest known pulsars, including the Guitar Nebula pulsar (PSR B2224+65), PSR B1953+50, PSR B1800-21, PSR B1757-24 and PSR B1610-50 all believed to have a velocity of $\gtrsim 1600$ km s^{-1} (see Cordes & Chernoff 1998; Caraveo 1993). In the case that the pulsar is much older than 11 kyr, IC cooling may play an important role for the oldest electrons, i.e.

those created nearest the place of birth, leading to strong energy-dependent morphology as observed here.

Adopting the kinematic distance of IRAS 13010−6254, the integrated γ-ray luminosity would represent about 28% of the current spin-down luminosity of the pulsar ($\dot{E}_{12.6} = \dot{E}/4\pi(12.6 \text{ kpc})^2 = 8.9 \times 10^{-11}$ erg cm^{-2} s^{-1}). This γ-ray conversion efficiency is higher than for typical PWNe ($\lesssim 10\%$ for PWNe with known γ-ray and X-ray luminosities, Mattana et al. 2009). However, high γ-ray conversion efficiency may not be unreasonable considering the very high "darkness ratio" of for this source of 156, which implies low synchrotron losses. Thus, an association of PSR J1301−6305 to the star forming region IRAS 13010−6254 cannot be ruled out, while the association is supported by the direction of the X-ray trail, the high ratio of N_H/DM, the large absolute value of N_H consistent with the entire integrated galactic column density in that direction, the possible bump seen in the TeV emission at the location of IRAS 13010−6254, the recent detection of IRAS 13010−6254 by Fermi as well as the high ratio of γ-ray to X-ray luminosity. This larger distance may also help explain the difficulty of detecting counterparts at other wavelengths.

8. Conclusions

PWNe now appear to constitute the largest class of Galactic VHE γ-ray emitters. The first dark source, and considered "prototypical" dark source, TeV J2032+4130 discovered by the HEGRA collaboration (Aharonian et al. 2002), was recently found to be "not-so-dark", after deeper X-ray and radio observations have revealed weak but significant counterparts (Butt et al. 2008) and the identification of a pulsar first in γ-rays (Abdo et al. 2009) and then in radio (Camilo et al. 2009). The work presented here has successfully identified energy-dependent morphology in VHE γ-rays as well as an X-ray PWN counterpart of HESS J1303−631, which now appears also to belong to the "not-so-dark", or "synchrotron under-luminous" class of VHE γ-ray sources having peak synchrotron energy fluxes that are much lower than the peak fluxes in the VHE regime. The observations presented here support the interpretation of this source as a large cloud of electrons, accelerated by the pulsar, which emit γ-ray radiation through the IC mechanism. These electrons can have an IC emission lifetime of the order of the pulsar age, and can, therefore, reflect the total energy output of the pulsar since birth, while the X-ray part of the PWN, generated by higher energy synchrotron emitting electrons with a much shorter interaction time, decreases rapidly in time and reflects only the more recent spin-down power of the pulsar (de Jager et al. 2009). While an association of the pulsar with the star formation region IRAS 13010−6254 is far from clear, it has been shown that it at least cannot be ruled out. The larger distance obtained from IRAS 13010−6254 may explain the very high absorption column density obtained from X-rays. The pulsar's true age, distance and origin remain open questions, as well as the details of the underlying electron populations that are responsible for the multi-wavelength emission. Current efforts to extend the radio and X-ray measurements of this source will be crucial for a deeper understanding of the processes at play.

Many other extended Galactic γ-ray sources which were previously unidentified are also finding associations with pulsars and PWNe as this class of sources continues to expand. The results obtained here also support the hypothesis that this "not-so-dark" source may be understood in the context of very low magnetic field, possibly in combination with a large distance to the source, causing relative extinction of the X-ray counterpart.

References

Abdo, A. A., Ackermann, M., Ajello, M., et al. 2009, ApJS, 183, 46
Abramowski et al. (H.E.S.S. collaboration) 2011, A&A, 533, A103
Aharonian, F. A., & Atoyan, A. M. 1999, A&A, 351, 330
Aharonian et al. (HEGRA collaboration) 2002, A&A, 393, L37
Aharonian et al. (H.E.S.S. collaboration) 2005a, A&A, 442, 1
Aharonian et al. (H.E.S.S. collaboration) 2005b, A&A, 439, 1013
Aharonian et al. (H.E.S.S. collaboration) 2006a, A&A, 460, 365
Aharonian et al. (H.E.S.S. collaboration) 2006b, A&A, 457, 899
Aharonian et al. (H.E.S.S. collaboration) 2008, A&A, 477, 353
Alpar, M. A., & Baykal, A. 2006, MNRAS, 372, 489
Arzoumanian, Z., Chernoff, D. F., & Cordes, J. M. 2002, ApJ, 568, 289
Becker, W., Kramer, M., Jessner, A., et al. 2006, ApJ, 645, 1421
Berge, D., Funk, S., & Hinton, J. 2007, A&A, 466, 1219
Bernlöhr, K., Carrol, O., Cornils, R., et al. 2003, Astropart. Phys., 20, 111
Blondin, J. M., Chevalier, R. A., & Frierson, D. M. 2001, ApJ, 563, 806
Brand, J., & Blitz, L. 1993, A&A, 275, 67
Bronfman, L., Nyman, L.-A., & May, J. 1996, A&AS, 115, 81
Butt, Y. M., Combi, J. A., Drake, J., et al. 2008, MNRAS, 385, 1764
Camilo, F., Ray, P. S., Ransom, S. M., et al. 2009, ApJ, 705, 1
Caraveo, P. A. 1993, ApJ, 415, L111
Condon, J. J., Griffith, M. R., & Wright, A. E. 1993, AJ, 106, 1095
Cordes, J. M., & Chernoff, D. F. 1998, ApJ, 505, 315
Cordes, J. M., & Lazio, T. J. W. 2002 [arXiv:astro-ph/0207156]
Cornils, R., Gillessen, S., Jung, I., et al. 2003, Astropart. Phys., 20, 129
Crawford, F., & Tiffany, C. L. 2007, AJ, 134, 1231
de Jager, O. C., Ferreira, S. E. S., Djannati-Ataï, A., et al. 2009, Proc. of the 31st ICRC, Lodz, Poland
Dickey, J. M., & Lockman, F. J. 1990, ARA&A, 28, 215
Dupays, A., Rizzo, C., & Bignami, G. F. 2010 [arXiv:1010.0597]
Espinoza, C. M., Lyne, A. G., Kramer, M., Manchester, R. N., & Kaspi, V. M. 2011, ApJ, 741, L13
Funk, S., Hermann, G., Hinton, J., et al. 2004, Astropart. Phys., 22, 285
Gaensler, B. M., & Frail, D. A. 2000, Nature, 406, 158
Gaensler, B. M., van der Swaluw, E., Camilo, F., et al. 2004, ApJ, 616, 383
Giacani, E., Smith, M. J. S., Dubner, G., & Loiseau, N. 2011, A&A, 531, A138
Hinton, J. A. 2004, New Astron. Rev., 48, 331
Lyne, A. G., Pritchard, R. S., Graham-Smith, F., & Camilo, F. 1996, Nature, 381, 497
Manchester, R. N., & Taylor, J. H. 1977, Pulsars, 36
Manchester, R. N., Hobbs, G. B., Teoh, A., & Hobbs, M. 2005, AJ, 129, 1993
Mattana, F., Falanga, M., Götz, D., et al. 2009, ApJ, 694, 12
Migliazzo, J. M., Gaensler, B. M., Backer, D. C., et al. 2002, ApJ, 567, L141
Moskalenko, I. V., Strong, A. W., Ormes, J. F., & Potgieter, M. S. 2002, ApJ, 565, 280
Mukherjee, R., & Halpern, J. P. 2005, ApJ, 629, 1017
Ohm, S., van Eldik, C., & Egberts, K. 2009, Astropart. Phys., 31, 383
Reid, M. J., Menten, K. M., Zheng, X. W., et al. 2009, ApJ, 700, 137
Ripken, J., Beilicke, M., Heinzelmann, G., & Horns, D. 2008, Proc. of the 30th ICRC (Mexico: Merida), 2, 795
Taylor, J. H., & Cordes, J. M. 1993, ApJ, 411, 674
Tibolla, O., Chaves, R. C. G., Domainko, W., et al. 2009 [arXiv:0912.3811]
Wang, Q. D., Lu, F. J., & Gotthelf, E. V. 2006, MNRAS, 367, 937
Watson, M. G., Schröder, A. C., Fyfe, D., et al. 2009, A&A, 493, 339
Wu, J. H. K., Wu, E. M. H., Hui, C. Y., et al. 2011, ApJ, 740, L12

[1] Universität Hamburg, Institut für Experimentalphysik, Luruper Chaussee 149, 22761 Hamburg, Germany
[2] Laboratoire Univers et Particules de Montpellier, Université Montpellier 2, CNRS/IN2P3, CC 72, Place Eugène Bataillon, 34095 Montpellier Cedex 5, France
[3] Max-Planck-Institut für Kernphysik, PO Box 103980, 69029 Heidelberg, Germany
[4] Dublin Institute for Advanced Studies, 31 Fitzwilliam Place, Dublin 2, Ireland
[5] National Academy of Sciences of the Republic of Armenia, Yerevan, Armenia
[6] Yerevan Physics Institute, 2 Alikhanian Brothers St., 375036 Yerevan, Armenia
[7] Universität Erlangen-Nürnberg, Physikalisches Institut, Erwin-Rommel-Str. 1, 91058 Erlangen, Germany
[8] University of Durham, Department of Physics, South Road, Durham DH1 3LE, UK
[9] Nicolaus Copernicus Astronomical Center, ul. Bartycka 18, 00-716 Warsaw, Poland
[10] CEA Saclay, DSM/IRFU, 91191 Gif-Sur-Yvette Cedex, France
[11] APC, AstroParticule et Cosmologie, Université Paris Diderot, CNRS/IN2P3, CEA/lrfu, Observatoire de Paris, Sorbonne Paris Cité, 10 rue Alice Domon et Léonie Duquet, 75205 Paris Cedex 13, France
[12] Laboratoire Leprince-Ringuet, École Polytechnique, CNRS/IN2P3, 91128 Palaiseau, France
[13] Institut für Theoretische Physik, Lehrstuhl IV: Weltraum und Astrophysik, Ruhr-Universität Bochum, 44780 Bochum, Germany
[14] Institut für Physik, Humboldt-Universität zu Berlin, Newtonstr. 15, 12489 Berlin, Germany
[15] LUTH, Observatoire de Paris, CNRS, Université Paris Diderot, 5 place Jules Janssen, 92190 Meudon, France
[16] LPNHE, Université Pierre et Marie Curie Paris 6, Université Denis Diderot Paris 7, CNRS/IN2P3, 4 place Jussieu, 75252 Paris Cedex 5, France
[17] Institut für Astronomie und Astrophysik, Universität Tübingen, Sand 1, 72076 Tübingen, Germany
[18] Astronomical Observatory, The University of Warsaw, Al. Ujazdowskie 4, 00-478 Warsaw, Poland
[19] Unit for Space Physics, North-West University, 2520 Potchefstroom, South Africa
[20] Landessternwarte, Universität Heidelberg, Königstuhl, 69117 Heidelberg, Germany
[21] Oskar Klein Centre, Department of Physics, Stockholm University, Albanova University Center, 10691 Stockholm, Sweden
[22] University of Namibia, Department of Physics, Private Bag 13301, Windhoek, Namibia
[23] UJF-Grenoble 1/CNRS-INSU, Institut de Planétologie et d'Astrophysique de Grenoble (IPAG) UMR 5274, 38041 Grenoble, France
[24] Department of Physics and Astronomy, The University of Leicester, University Road, Leicester, LE1 7RH, UK
[25] Instytut Fizyki Jądrowej PAN, ul. Radzikowskiego 152, 31-342 Kraków, Poland
[26] Institut für Astro- und Teilchenphysik, Leopold-Franzens-Universität Innsbruck, 6020 Innsbruck, Austria
[27] Laboratoire d'Annecy-le-Vieux de Physique des Particules, Univ. de Savoie, CNRS/IN2P3, 74941 Annecy-le-Vieux, France
[28] Obserwatorium Astronomiczne, Uniwersytet Jagielloński, ul. Orla 171, 30-244 Kraków, Poland
[29] Toruń Centre for Astronomy, Nicolaus Copernicus University, ul. Gagarina 11, 87-100 Toruń, Poland
[30] School of Chemistry & Physics, University of Adelaide, Adelaide 5005, Australia
[31] Charles University, Faculty of Mathematics and Physics, Institute of Particle and Nuclear Physics, V Holešovičkách 2, 180 00 Prague 8, Czech Republic
[32] School of Physics & Astronomy, University of Leeds, Leeds LS2 9JT, UK
[33] Université Bordeaux 1, CNRS/IN2p3, Centre d'Études Nucléaires de Bordeaux Gradignan, 33175 Gradignan, France
   e-mail: dalton@cenbg.in2p3.fr
[34] European Associated Laboratory for Gamma-Ray Astronomy, jointly supported by CNRS and MPG